Nanoscale

A High-Efficiency and Long-Cycling Aqueous Indium Metal Battery Enabled by Synergistic In3+/K+ Interactions

Journal:	*Nanoscale*
Manuscript ID	NR-ART-07-2024-002905.R1
Article Type:	Paper
Date Submitted by the Author:	10-Nov-2024

Complete List of Authors:	Chang, Songyang; University of Puerto Rico Rio Piedras, Department of Chemistry Hou, Wentao; University of Puerto Rico Rio Piedras, Department of Chemistry Conde-Delmoral, Amanda; University of Puerto Rico Rio Piedras, Department of Chemistry Ullah, Irfan; University of Puerto Rico Rio Piedras, Department of Chemistry Florez Gomez, Jose Fernando; University of Puerto Rico Rio Piedras, Department of Physics Morell, Gerardo; University of Puerto Rico Rio Piedras, Department of Physics Wu, Xianyong; University of Puerto Rico Rio Piedras, Department of Chemistry

ARTICLE

A High-Efficiency and Long-Cycling Aqueous Indium Metal Battery Enabled by Synergistic In^{3+}/K^+ Interactions

Received 00th January 20xx,
Accepted 00th January 20xx

DOI: 10.1039/x0xx00000x

Songyang Chang,[a] Wentao Hou,[a] Amanda Conde-Delmoral,[a] Irfan Ullah,[a] Jose Fernando Florez Gomez,[b] Gerardo Morell,[b] and Xianyong Wu*[a]

Aqueous trivalent metal batteries are promising options for energy storage, owing to their ability to transfer three electrons during redox reactions. However, advances in this field have been limited by challenges such as incompatible M^{3+}/M electrode potentials and salt hydrolysis. Herein, we identify trivalent indium metal as a viable candidate and demonstrate a high-performance indium-Prussian blue hybrid battery using a K^+/In^{3+} mixture electrolyte. Interestingly, there exists a synergistic interaction between K^+ and In^{3+} ions, which enhances the Coulombic efficiency and prolongs the cycling life. Specifically, the addition of K^+ elevates the In^{3+}/In plating efficiency from 99.3% to 99.6%, due to the decreased electrolyte acidity and enlarged indium particle size. Simultaneously, the presence of In^{3+} creates an inherently acidic environment (pH~3.1), which effectively stabilizes K^+ insertion into the Prussian blue framework. Consequently, this hybrid battery delivered a high capacity of 130 mAh g^{-1}, an exceptional rate of 96 A g^{-1} (~740 C), and extraordinary cycling life of 48,000 cycles. This work offers an innovative approach to develop high-performance hybrid metal batteries.

Introduction

The development of next-generation battery systems has garnered significant attention, because conventional lithium-ion batteries face challenges in terms of limited resources, high cost, and safety issues.[1-3] Recently, aqueous rechargeable batteries have emerged as a competitive contender in the energy storage landscape, due to their intrinsic nonflammability, low cost, and environmental friendliness.[4-10] Particularly, aqueous multivalent metal batteries represent a mainstream research direction, due to ultrahigh capacities in metal electrodes (450-960 mAh g^{-1}) and resultant high energy density.[11-16] For instance, zinc (Zn) batteries have attracted extensive interest from worldwide researchers, owing to the high capacity (820 mAh g^{-1}), low potential (-0.76 V *vs.* standard hydrogen electrode, SHE), and low price of Zn metal.[17-19] However, the dendrite formation, hydrogen evolution reaction (HER), and electrode passivation significantly retard the development of Zn batteries.[20-24] Therefore, there is an emerging trend to develop novel metal batteries to circumvent these challenges.

Recently, researchers have started to evaluate other divalent transition metals, such as iron,[25-28] nickel,[29,30] manganese,[31-34] and copper,[35-39] as alternative post-zinc battery systems. Nevertheless, much less attention has been paid to trivalent metals (aluminum, gallium, indium, antimony, bismuth), despite their intriguing three-electron transfer reactions with notably high capacities. Among them, aluminum (Al) stands out due to its predominantly high capacity (2980 mAh g^{-1}); however, the very low Al^{3+}/Al potential (-1.66 V *vs.* SHE) leads to significant water decomposition, posing a considerable challenge.[40,41] Other candidates, including gallium (Ga^{3+}), antimony (Sb^{3+}), and bismuth (Bi^{3+}), exhibit higher redox potentials, but they rapidly undergo hydrolysis reactions in aqueous solutions.[42-44] Hence, incompatible redox potentials and ion hydrolysis reactions constitute two major challenges for aqueous trivalent metal batteries.

In comparison, indium (In) is a feasible trivalent metal choice, which not only possesses a moderate redox potential (-0.34 V *vs.* SHE) but also exhibits high solubility in water without hydrolysis.[45] Besides, it offers a substantial capacity of ~700 mAh g^{-1} by virtue of its 3-electron reaction, approaching that of Zn. Lastly, In metal demonstrates a spherical, micron-sized, and dendrite-free plating morphology, leading to a high Coulombic efficiency of 99.3% in a pristine 1 M $InCl_3$ electrolyte.[45] When combined with a low-cost manganese dioxide cathode, the full cell realized a stable cycling for 680 cycles. All these results motivate us to further investigate and fine-tune In metal battery performance, particularly regarding the enhancement of In plating efficiency and the development of long-cycling cathode materials.

In this study, we present a high-performance hybrid In metal battery based on the indium-Prussian blue analogue (PBA) reaction chemistry in a hybrid K^+/In^{3+} electrolyte. Importantly, the synergistic effect between In^{3+} and K^+ ions significantly enhances the performance of both the In anode and the PBA cathode. Specifically, the introduction of K^+ decreases the acidity of the In^{3+} electrolyte and promotes the formation of larger In particles, thus raising the In plating efficiency from 99.3% to 99.6%. Meanwhile, the presence of In^{3+} maintains a moderately acidic environment (pH~3.1) and thus stabilizes K^+ insertion into the PBA cathode, which increases the capacity

[a] *Department of Chemistry, University of Puerto Rico-Rio Piedras Campus, San Juan, PR 00925-2537, USA*
[b] *Department of Physics, University of Puerto Rico-Rio Piedras Campus, San Juan, PR, 00925-2537, USA*
† Corresponding author: Xianyong Wu (xianyong.wu@upr.edu)
Supplementary Information available: [details of any supplementary information available should be included here]. See DOI: 10.1039/x0xx00000x

retention from 6.45% to 70% after 2000 cycles. Benefitting from this synergistic interaction, the hybrid battery exhibits a superior cycling performance, with 80.7% retention over 10,000 cycles and 51.5% over 48,000 cycles. Additionally, it supports an ultrahigh rate capability of 96 A g^{-1} (~740 C), due to the fast K^+ insertion on the cathode and rapid In^{3+} plating on the anode.

Results and Discussion

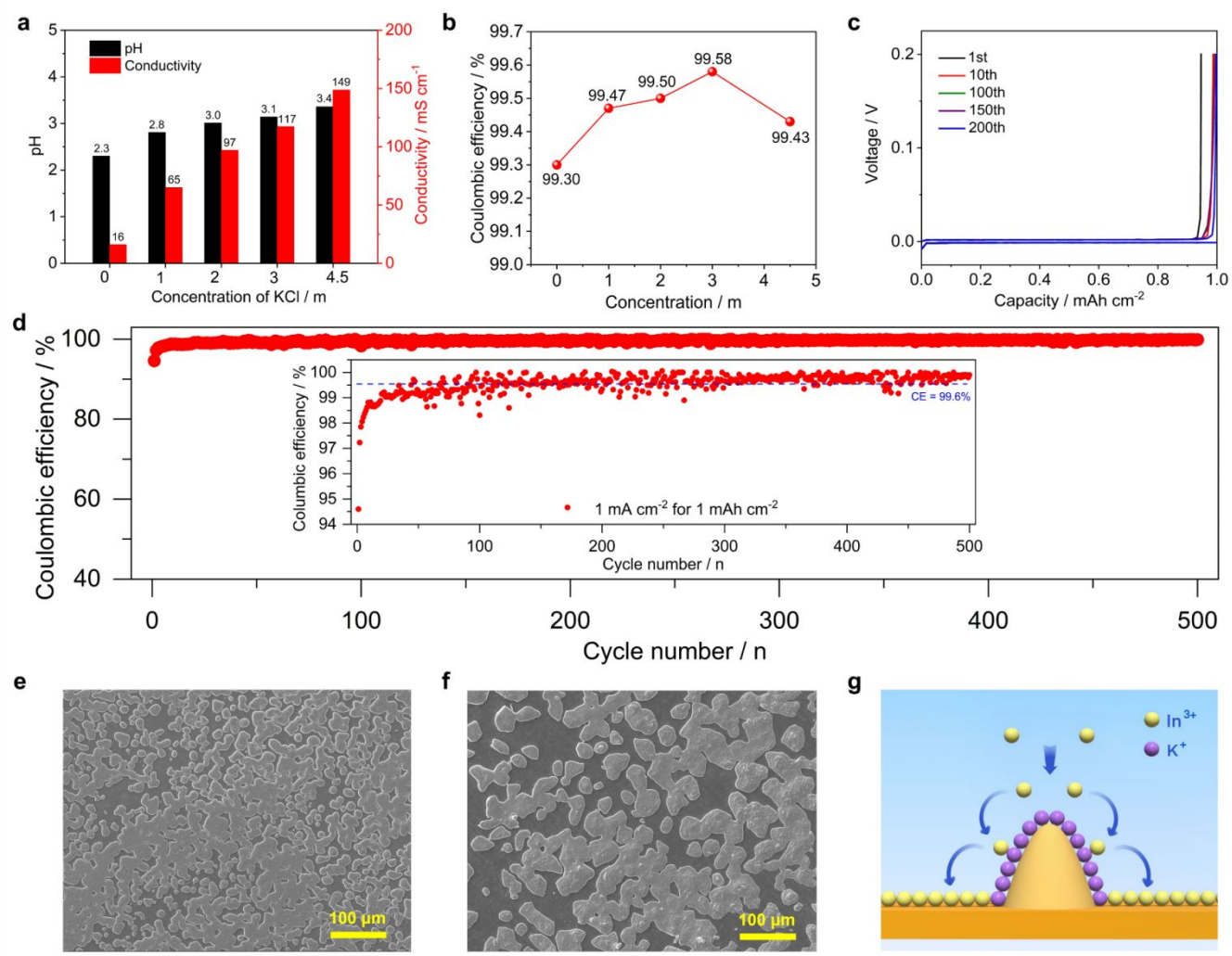

Figure 1. Physical and electrochemical characterizations of the 1.0 m $InCl_3$ + X m KCl electrolyte (X = 0, 1, 2, 3, and 4.5): (a) The ionic conductivity and pH values; (b) The average plating efficiency; (c) GCD curves of the In||Ti battery in the 1 m $InCl_3$ + 3 m KCl electrolyte; (d) The Coulombic efficiency during cycling; (e) The SEM image of the plated In metal in the pristine 1 m $InCl_3$ electrolyte; (f) The SEM image of the plated In metal in the 1 m $InCl_3$ + 3 m KCl electrolyte; (g) The scheme of the electrostatic shielding mechanism. The testing condition is 1 mA cm^{-2} current for 1 mAh cm^{-2} capacity.

We aim to fabricate a potassium-based hybrid In metal battery, considering the potassium's high abundance, low cost, and high ionic conductivity in water.[46-48] We utilized 1.0 m (m: mol kg^{-1}) $InCl_3$ as the baseline electrolyte and studied the effect of KCl concentrations on the battery performance. Given that the maximal solubility of KCl in the hybrid electrolyte is 4.5 m (**Figure S1**), we designed 5 different electrolytes for initial screening: 1+0, 1+1, 1+2, 1+3, and 1+4.5 m.

Figure 1a shows the impact of KCl additives on the electrolyte properties (pH values and ionic conductivity). As the KCl concentration increases from 0 to 4.5 m, the ionic conductivity markedly rises from 16 mS cm^{-1} to 149 mS cm^{-1}. It is known that hydrated K^+ ions have a small Stokes radius,[49-51] leading to high mobility in aqueous electrolytes. Thus, adding K^+ can decrease the cell resistance and increase the battery rate performance. Meanwhile, the pH value progressively elevates from 2.3 to 3.4 with higher K^+ concentrations, suggesting reduced electrolyte acidity. The $[H^+]$ concentration has been decreased by an order of magnitude, because pH is the negative logarithm of proton concentrations (pH = -log$[H^+]$).[52] Of note, trivalent cations possess high charge density, resulting in strong Coulombic interactions with water molecules.[52] This interaction

promotes acidic conditions through the chemical equilibrium reaction: $[In(H_2O)_6]^{3+}(aq) + H_2O (l) \rightleftharpoons [In(H_2O)_5OH]^{2+} (aq) + H_3O^+ (aq)$.[52] When K^+ ions are introduced, the overall In^{3+} concentration is diluted and decreased, thus lowering the hydronium (H_3O^+) concentrations and increasing the pH value accordingly.

To evaluate the In plating efficiency, we assembled In||Ti batteries using a chemically stable titanium (Ti) foil as the substrate. **Figure 1b** shows the Coulombic efficiency with respect to KCl additives. Interestingly, all hybrid electrolytes exhibit higher efficiencies than the pristine $InCl_3$, and the best efficiency is achieved with an intermediate combination of 1 m $InCl_3$ + 3 m KCl (~99.6%). **Figure 1c** displays selected Galvanostatic charge/discharge (GCD) curves of this In||Ti battery in the optimal electrolyte, where well-defined plating/stripping curves and minimal polarization (~2.0 mV) are attainable. The initial efficiency is 94.6%, and it gradually increases to 98.7% in the 10th cycle, 99.5% in the 100th cycle, and reaches 99.7% in the 200th cycle. The cycling performance is presented in **Figure 1d**, wherein the battery demonstrates a long calendar life of 1000 hours with an average efficiency of ~99.6% over 500 cycles. GCD curves and cycling data for In||Ti batteries with other electrolytes are provided in **Figure S2-5**.

Compared with the pristine 1 m $InCl_3$, the 0.3% efficiency improvement in the 1+3 m electrolyte seems to be minor; however, for metal electrodes, efficiency directly reflects the reaction reversibility and thus plays a critical role in the full cell cycling. From another perspective, the reaction irreversibility has decreased from 0.7% to 0.4%, corresponding to 48% improvement. If we assume a full cell with 200 cycles, the capacity retention in the 1 m $InCl_3$ electrolyte will be $(0.993)^{200}$ = 24.5%. By contrast, the retention will be $(0.996)^{200}$ = 44.9% in the 1+3 m electrolyte, which is 83% higher than the pristine one.

The improved In plating efficiency can be attributed to two primary factors. Firstly, the introduction of K^+ ions elevated pH values of hybrid electrolytes (**Figure 1a**), thereby mitigating HER side reactions. Note that a higher pH value means lower $[H^+]$ concentrations, leading to a smaller probability of HER. Secondly, K^+ ions influenced the In plating morphology and profoundly increased the metal particle size, which minimized the electrode-electrolyte contact area and benefited the plating efficiency. **Figure 1e-f** and **Figure S6** show scanning electron microscopy (SEM) images of the plated In metals. As shown, the In particle size is ~20 µm in the pristine $InCl_3$, but it proliferates to 40-60 µm in the 3 m KCl electrolyte (**Figure 1f**). Larger particle sizes not only decrease the surface area but also enhance the interconnection between particles, suppressing side reactions and improving plating efficiency.[53]

Furthermore, we hypothesize that K^+ ions may exert an electrostatic shielding effect on the In plating (**Figure 1g**), a concept originally proposed for lithium (Li) metal but applicable to other metals.[54,55] Considering the significant difference in redox potentials between In^{3+}/In (-0.34 V) and K^+/K couples (-2.9 V), K^+ ions cannot be reduced in aqueous electrolytes and remain redox-inactive during plating. These positively charged K^+ ions will electrostatically absorb on the surface or tips of the growing In particles, which further repel the positive In^{3+} cations and promote them to plate in adjacent areas, eventually leading to a regulated morphology with larger sizes. Due to these beneficial effects, the In metal can sustain a promising efficiency of 98.7-99.2% at high plating capacity of 3-10 mAh cm^{-2} (**Figure S7**).

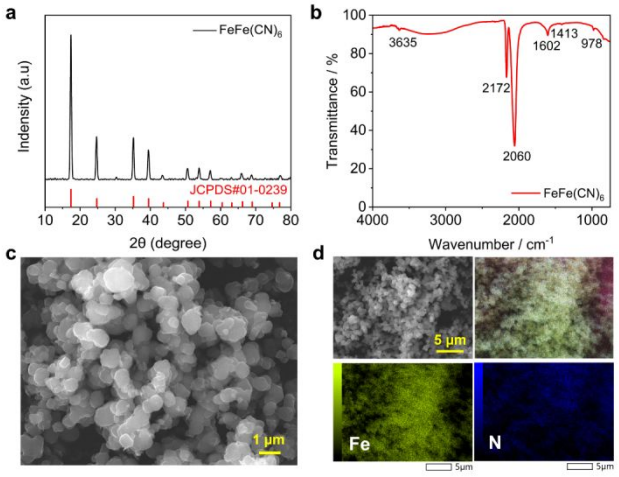

Figure 2. Physical characterizations of the $FeFe(CN)_6$ cathode. (a) The XRD pattern; (b) The FT-IR result; (c) The SEM image; (d) Elemental mapping results.

To fabricate a hybrid battery, it is essential to identify a high-capacity and long-cycling cathode material. Among various materials, Prussian Blue analogues (PBA) represent a promising option,[56] due to their easy synthesis, large-open crystal structures, fast ion insertion kinetics, and reversible redox behavior.[57,58] Particularly, PBA materials are well known for their ionic preference and selectivity in the sequence of $K^+ > Na^+ > Li^+$.[59] Consequently, K^+ insertion features an elevated reaction potential and extended cycling life. Herein, we selected a well-established iron-based PBA material of $FeFe(CN)_6$ as the K-insertion cathode.

This material was prepared by a simple aqueous precipitation method, [60-62] which shows a typical dark green color (**Figure S8**). **Figure 2a** shows its X-ray diffraction (XRD) pattern, which adopts a face-centered cubic structure (space group Fm-3m) with an index to the standard $Fe_4[Fe(CN)_6]_3$ compound (JCPDS#01-0239). The diffraction peaks are quite sharp and strong, and there are no extra peaks, indicating high crystalline and material purity. **Figure 2b** shows the Fourier-transform infrared spectroscopy (FT-IR) result of this material, wherein two strong peaks at 2172 cm^{-1} and 2060 cm^{-1} can be attributed to the Fe^{3+}-CN-Fe^{3+} and Fe^{3+}-CN-Fe^{2+} vibrations, respectively.[63] The stretching and bending of O-H bonds that belong to crystal water molecules are attributed to the 3635 cm^{-1} and 1602 cm^{-1} peaks, respectively.[64] **Figure 2c** displays a SEM image of the PBA material, which exhibits a regular quasi-cube morphology with an average size of ~500 nm. Energy dispersive spectra (EDS) mapping detects a relatively homogeneous elemental distribution in the

sample (**Figure 2d**), suggesting a high material purity.

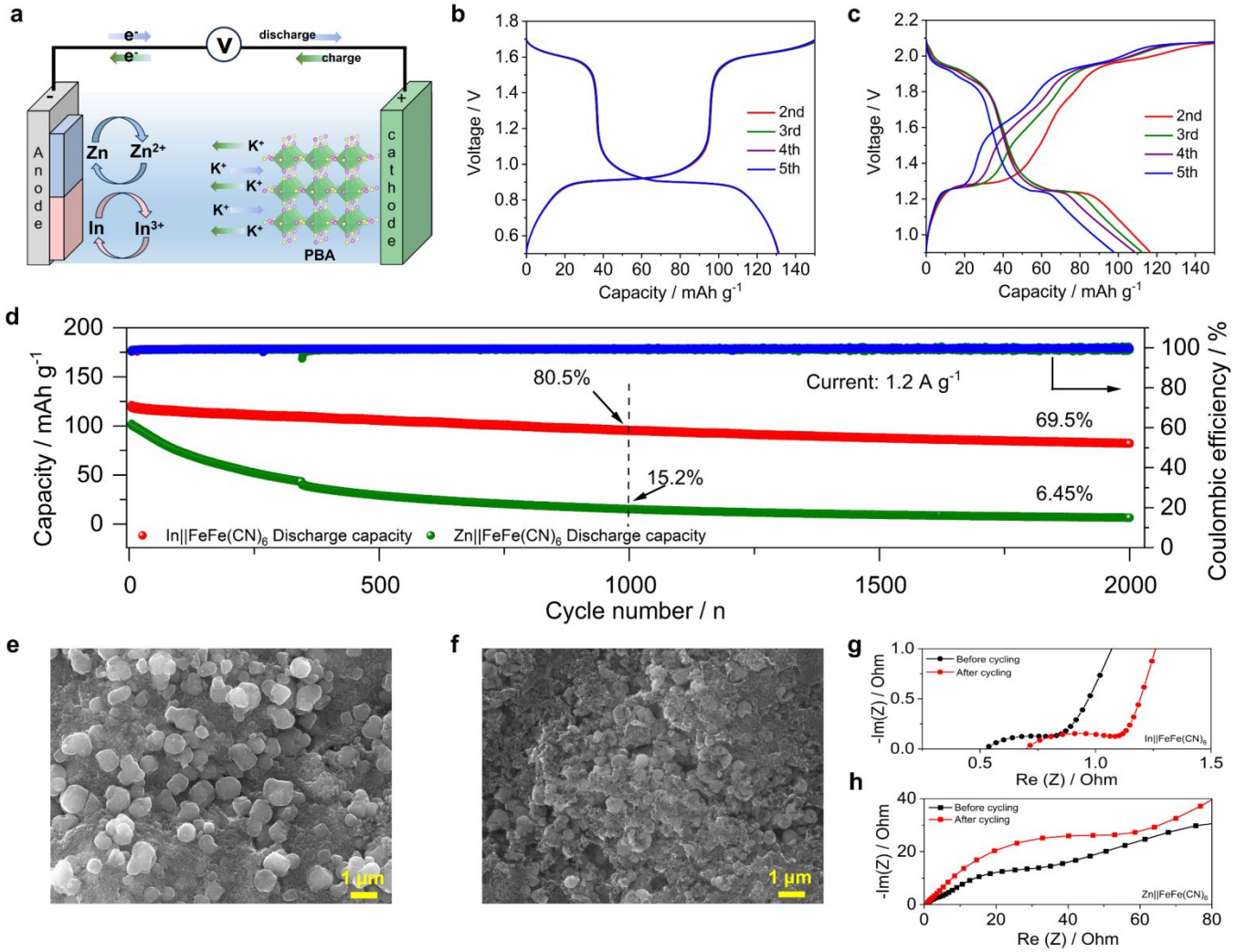

Figure 3. Electrochemical characterization of hybrid batteries. (a) The working mechanism; (b) GCD curves of the In||$FeFe(CN)_6$ battery at 120 mA g^{-1}; (c) GCD curves of the Zn||$FeFe(CN)_6$ battery at 120 mA g^{-1}; (d) The cycling performance comparison at 1.2 A g^{-1}; (e) The SEM image of the cycled electrode in the hybrid In batteries; (f) The SEM image of the cycled electrode in the hybrid Zn batteries; (g-h) The EIS comparison of the hybrid battery after cycling. The electrolyte is 1 m $InCl_3$ + 3 m KCl and 1 m $ZnCl_2$ + 3 m KCl for the hybrid In and Zn batteries.

To harness the superior performance of the In anode, we assembled an aqueous hybrid In||$FeFe(CN)_6$ battery. For comparative analysis, we also fabricated a hybrid Zn||$FeFe(CN)_6$ battery. **Figure 3a** schematically illustrates the working mechanism. The cathode preferentially works on K^+ insertion in the $FeFe(CN)_6$ framework, because PBA shows a high ionic selectivity toward bulky monovalent K^+ ions. Concurrently, the metal anode undergoes the In^{3+}/In or Zn^{2+}/Zn plating reaction, as K^+ ions cannot be reduced in water. Theoretically, the choice of the metal counter electrode should not significantly influence K^+ insertion in the cathode, especially considering the large excess of the metal anode (>100 mA cm^{-2}) and the ample electrolyte volume (~100 μL). Surprisingly, the In||$FeFe(CN)_6$ battery exhibits a superior cycling performance compared to Zn||$FeFe(CN)_6$, suggesting a synergistic interaction between In^{3+} and K^+ ions.

Figure 3b displays GCD curves of the In||$FeFe(CN)_6$ battery, which exhibits two distinct discharge plateaus at ~1.6 V and 0.85 V, corresponding to the redox reaction of carbon-coordinated and nitrogen-coordinated Fe^{3+}/Fe^{2+} couples, respectively. The GCD curves are highly consistent and overlap well, and they resemble those in a pure 3 m KCl electrolyte (**Figure S9**), indicating K^+ insertion in the cathode structure. The battery delivers a discharge capacity of ~131 mAh g^{-1}, leading to a specific energy of 141.7 Wh kg^{-1} based on the cathode active mass. In contrast, the Zn-based hybrid battery demonstrates similar GCD curves (**Figure 3c**) with two higher discharge plateaus at ~1.9 and 1.25 V, attributed to the lower Zn^{2+}/Zn redox potential. Despite higher voltages, the Zn||$FeFe(CN)_6$ battery encounters a notable capacity within the first few cycles.

The In||$FeFe(CN)_6$ battery achieves a much better cycling performance than the Zn-based one, highlighting a high compatibility between the In anode and $FeFe(CN)_6$ cathode. **Figure 3d** illustrates the cycling stability of both systems. The In battery fades from 118 mAh g^{-1} to 95 mAh g^{-1} after 1000 cycles, corresponding to a capacity retention of 80.5%. After 2000 cycles, the In battery still maintains ~70% of its original capacity. In stark contrast, the Zn||$FeFe(CN)_6$ battery suffers from drastic capacity fading, with a low capacity retention of ~15.2% after 1000 cycles and 6.5% after 2000 cycles. **Figure S10** provides the selected GCD curves during cycling for further insights.

To understand the performance disparity, we conducted *ex-situ* SEM and electrochemical impedance spectra (EIS) analyses after 500 cycles at 1.2 A g^{-1}. **Figure 3e** shows the SEM image of the $FeFe(CN)_6$ cathode in the In^{3+}/K^+ electrolyte, which well retains its original quasi-cube features without noticeable size or morphology changes. Nevertheless, this $FeFe(CN)_6$ cathode experiences an evident morphology change and size decrement in the Zn^{2+}/K^+ electrolyte (**Figure 3f**), suggesting significant material degradation. EIS studies provide further evidence for their performance differences. As shown in **Figure 3g**, the In||$FeFe(CN)_6$ battery exhibits a stable charge-transfer resistance, remaining almost unchanged from ~0.41 ohms before cycling to ~0.42 ohms after cycling. This stability indicates a robust insertion process. However, the Zn||$FeFe(CN)_6$ battery shows a substantial increase in charge-transfer resistance, rising from ~42.0 ohms to ~72.5 ohms after cycling, reflecting deteriorated electrochemical performance (**Figure 3h**).

We reason that the better cycling in the In||$FeFe(CN)_6$ battery may come from two aspects. Firstly, In^{3+} ions are more densely charged, leading to a more acidic environment than Zn^{2+} electrolytes. As tested, the pH value for the In^{3+}/K^+ and Zn^{2+}/K^+ electrolyte is 3.1 and 5.4, respectively. It is well documented that PBA materials favor acidic electrolytes for stable cycling. For instance, Cui *et al.* reported an outstanding cycling life (40,000 cycles) for the $KCuFe(CN)_6$ cathode in an acid-assisted K^+ electrolyte (pH~2.0).[65] Secondly, there may exist a crosstalk effect between the cathode and anode. The Zn||$FeFe(CN)_6$ battery is more susceptible to side reactions at the anode. Particularly, Zn likely triggers substantial HER side reactions and generate hydroxide (OH^-) ions.[66] It is plausible that some OH^- anions diffuse to the vicinity of the $FeFe(CN)_6$ cathode, contributing to its morphology change and resistance increment. In contrast, the In||$FeFe(CN)_6$ system avoids these issues, as In resists such side reactions and features high efficiency (99.6%), thereby preserving the structural and morphology integrity of the cathode.

The In||$FeFe(CN)_6$ hybrid battery exhibits remarkable ultrahigh-rate capability and exceptional cycling life, distinguishing itself as a superior energy storage solution. As shown in **Figure 4a** and **Figure S11**, the discharge capacity is 106, 102, 93, 86, 80, 77, 69, 64 and 56 mAh g^{-1} at 0.6, 1.2, 3.6, 6, 9.6, 12, 24, 36, and 60 A g^{-1}, respectively. Even at a very high rate of 96 A g^{-1}, the battery still retains a good capacity of 46 mAh g^{-1}, corresponding to a capacity utilization of 43%. Of note, the 96 A g^{-1} current corresponds to a very high rate of ~740 C (1 C = 130 mA g^{-1}), meaning that the charge or discharge time is as short as ~4.9 seconds. Based on these GCD curves, we plotted the Ragone curve to show the energy-power relationship. As shown in **Figure S12**, the specific energy is 115.2 Wh kg^{-1} at 651 W kg^{-1}, which still reaches 33.2 Wh kg^{-1} at a high-power of 70348.6 W kg^{-1}.

Such an excellent rate performance can be attributed to several factors. Firstly, the hybrid electrolyte inherits the high ionic conductivity of K^+ ions, which exhibits a high conductivity of 117 mS cm^{-1} and thus benefits the rate performance. Secondly, the In metal anode demonstrates fast plating/stripping kinetics. In symmetrical In||In batteries (**Figure S13**), the polarization remains remarkably low at approximately 1.5 mV, indicating very fast electrochemical reaction kinetics. Therefore, we tested its rate properties at higher currents. As shown in **Figure 4b** and **Figure S14**, the polarization value is 2.5, 6.5, 13, 16, 30, 44, 106 and 130 mV at 2, 5, 8, 10, 30, 50, 80 and 100 mA cm^{-2}, respectively. Thirdly, the PBA cathode features a quasi-capacitive ion insertion process. We tested cyclic voltammetry (CV) curves of the In||$FeFe(CN)_6$ battery at various scanning rates. At 1 mV s^{-1}, two pairs of oxidization/reduction peaks are observed at 0.93/1.64 and 0.89/1.59 V, corresponding to the redox of carbon-coordinated and nitrogen-coordinated Fe^{3+}/Fe^{2+} couples. As the scanning rate increases, the cathodic and anodic peak intensities proliferate accordingly (**Figure 4c**). By analyzing the relationship between the logarithm of the peak current [log(i)] and the scanning rate [log(v)], we can derive a slope rate as 0.642 and 0.663 for the cathodic and anodic peaks, respectively (**Figure S15**). These values fall between 0.5 and 1, suggesting a partially capacitive insertion process. Among these factors, the cathode structure should play a major role. In our previous work, [60] the $FeFe(CN)_6$ cathode also exhibited an ultrahigh rate capability up to 100 A g^{-1} in the pristine K_2SO_4 electrolyte.

Besides the high rate, the hybrid battery delivers an extraordinary cycling life at high current densities. As shown in **Figure 4e**, the capacity retention is 80.7%, 66.7%, and 57.3% after 10000, 20000, and 30000 cycles. After 48000 cycles, the capacity retention is 51.6%. **Figure S16** shows selected GCD curves during the long-term cycling. *Ex-situ* SEM characterizations reveal the reversible insertion/extraction of K^+ ions in the $FeFe(CN)_6$ framework (**Figure S17-18**), which contributes to the stable cycling life.

To our knowledge, this cycling number has far exceeded the performance for other $FeFe(CN)_6$ based batteries, including Li^+, Na^+, K^+, and NH_4^+, [60,61,64,67-75] as compared in **Table S1**. To further push the limit of the cycling life, we assembled a hybrid full cell with a limited negative/positive (N/P) capacity ratio of 2:1. This N/P ratio is higher than conventional lithium-ion batteries (1.05-1.1), but it is reasonable in metal based full cells,[76,77] because metal electrodes usually exhibit moderate Coulombic efficiencies.

The cathode exhibits a moderately high active mass loading of ~5 mg cm^{-2}, leading to an area capacity of ~0.6 mAh cm^{-2}. The In anode is pre-deposited on the Ti foil with a controlled capacity of 1.2 mAh cm^{-2}. As shown in **Figure 4f** and **Figure S19**, this full cell capacity decreases from 107 to 89.5 mAh g^{-1} after 700 cycles, corresponding to a promising retention rate of 83.6%. The average Coulombic efficiency for this hybrid cell is 98.7%. These results clearly indicate the promise of hybrid In metal batteries for energy storage.

Despite these promising cell performances, there are some notable challenges that need to be addressed in future studies. For instance, the K^+/In^{3+} ion concentrations in the hybrid electrolyte will change with the charge/discharge states, especially when the electrode area capacity is high in practical applications. To mitigate this issue, a relatively flooded electrolyte configuration could be used, which can store more ions in the liquid form. In addition, indium is a rare element on Earth, which may restrict its large-scale applications. Therefore, we propose that indium metal batteries might be used in specific cases that prioritize performance than cost, such as miniature applications. For instance, the commercial zinc-silver oxide battery utilizes a rare and expensive silver element, due to the highly stable voltage and high density of the silver oxide. It is possible that indium metal batteries could be suitable for wearable devices that require high safety, high performance, and a small battery size (minimal usage of indium).

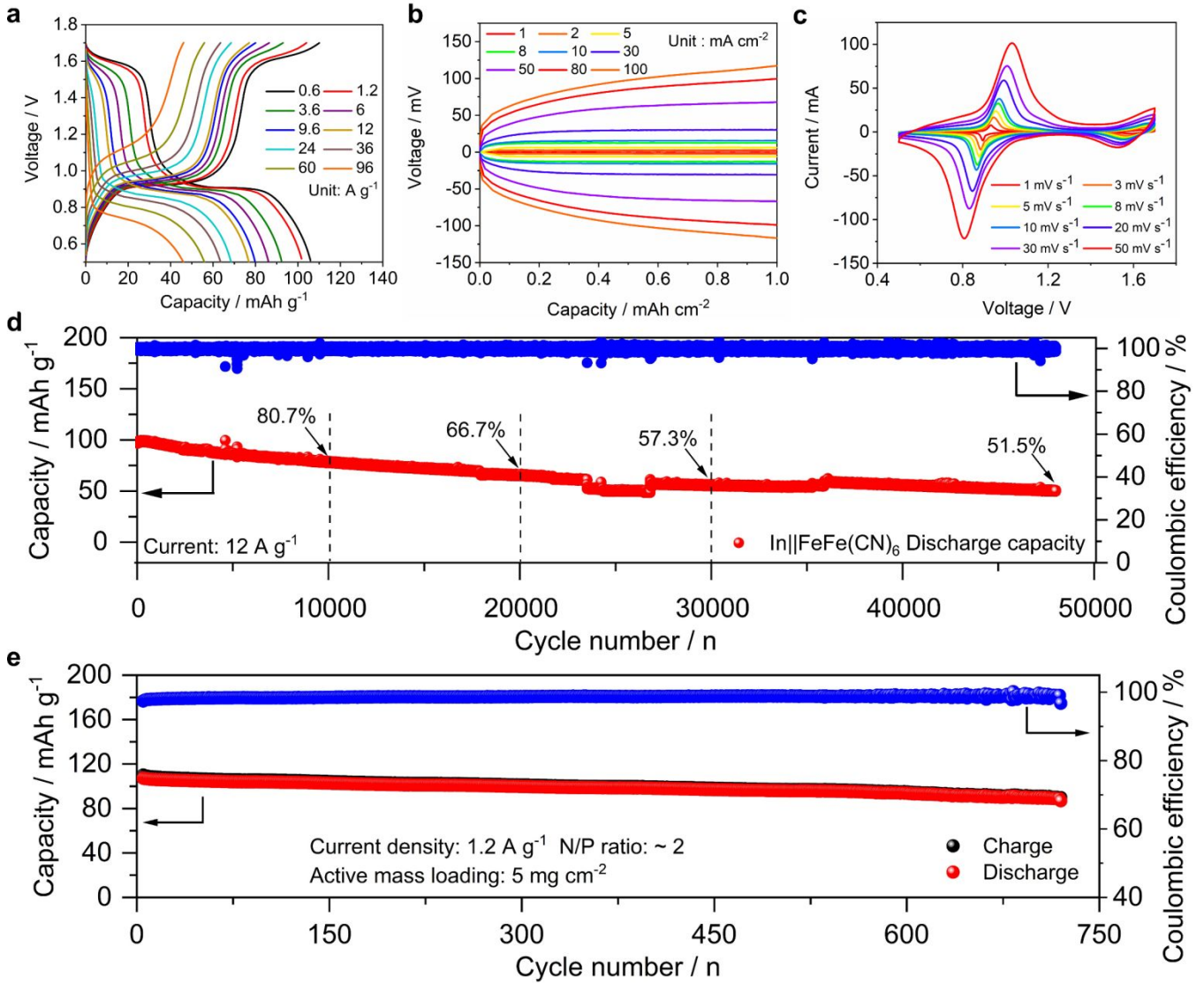

Figure 4. Electrochemical characterization of the In||$FeFe(CN)_6$ hybrid battery. (a) The rate performance; (b) GCD curves of the symmetrical In||In battery at different current densities; (c) CV curves at different scanning rates; (d) The cycling performance at 12 A g^{-1}; (e) The cycling performance of the hybrid full cell at 1.2 A g^{-1}.

Conclusions

We developed a high-performance hybrid In metal battery based on a $FeFe(CN)_6$ cathode, an In metal anode, and a mixture In^{3+}/K^+ electrolyte. Interestingly, there exists a synergistic effect between In^{3+} and K^+ ions, leading to

enhanced In plating efficiency (99.7%) on the anode and stabilized K^+ insertion reaction (51.6% over 48,000 cycles) on the cathode. Besides, the fast K^+ insertion and In^{3+} plating kinetics concurrently contribute to its ultrahigh rate performance, where 43.4% capacity can be maintained at ~740 C rate (96 A g^{-1}). This work provides a promising approach to build fast-charging and long-cycling aqueous trivalent metal batteries for energy storage.

Author contributions

All authors have given the permission for the final version of this manuscript. Conceptualization: X. Wu; data curation and formal analysis: S. Chang, W. Hou, A. Conde-Delmoral, I. Ullah, J. Fernando Florez Gomez; visualization: X. Wu; resources: G. Morell and X. Wu; writing – original draft, review, and editing: S. Chang and X. Wu.

Conflicts of interest

There are no conflicts to declare.

Data availability

The data supporting this article have been included as part of the Supplementary Information.

Acknowledgements

The authors are grateful to Jiayi Xue in Konkuk University for her help with the preparation of figure 1g in this paper. The authors thank the financial support from the NSF Center for the Advancement of Wearable Technologies (grant no. 1849243) and NASA MIRO PR-SPRInT (grant no. 80NSSC19M0236).

Notes and references

1 A. Innocenti, D. Bresser, J. Garche and S. Passerini, *Nat. Commun.*, 2024, **15**, 4068.
2 X. Ji, *Energy Environ. Sci.*, 2019, **12**, 3203-3224.
3 Z. Shang, S. Wang, H. Zhang, W. Zhang, S. Lu and K. Lu, *Nanoscale*, 2022, **14**, 14433-14454.
4 J. Shin and J. W. Choi, *Adv. Energy Mater.*, 2020, **10**, 2001386.
5 L. Li, Q. Zhang, B. He, R. Pan, Z. Wang, M. Chen, Z. Wang, K. Yin, Y. Yao and L. Wei, *Adv. Mater.*, 2022, **34**, 2104327.
6 G. Liang, F. Mo, X. Ji and C. Zhi, *Nat. Rev. Mater.*, 2021, **6**, 109-123.
7 S. Chang, S. Qiu, S. Katiyar, J. F. Florez Gomez, Z. Feng and X. Wu, *Batteries*, 2023, **9**, 349.
8 N. Fu, Y.-T. Xu, S. Zhang, Q. Deng, J. Liu, C.-J. Zhou, X.-W. Wu, Y.-G. Guo and X.-X. Zeng, *J. Energy Chem.*, 2022, **67**, 563-584.
9 X. Zhao, Z. Zhao‐Karger, M. Fichtner and X. Shen, *Angew. Chem. Int. Ed.*, 2020, **59**, 5902-5949.
10 Y. Zhu, R. Zhu, F. Chen, S. Zhang, Y. C. Kuo, P. Guan, M. Li, Y. Liu, Z. Han and T. Wan, *Energy Environ. Mater.*, 2024, **7**, e12493.
11 S. Qiu, M. Lucero, X. Wu, Q. Wang, M. Wang, Y. Wang, W. S. Samarakoon, M. R. Bolding, Z. Yang and Y. Huang, *ACS Mater. Au*, 2021, **2**, 63-71.
12 L. Ma, Q. Li, Y. Ying, F. Ma, S. Chen, Y. Li, H. Huang and C. Zhi, *Adv. Mater.*, 2021, **33**, 2007406.
13 H. Jiang, L. Tang, Y. Fu, S. Wang, S. K. Sandstrom, A. M. Scida, G. Li, D. Hoang, J. J. Hong and N.-C. Chiu, *Nat. Sustain.*, 2023, 1-10.
14 S. Chang, L. Lu, I. Ullah, W. Hou, J. F. Florez Gomez, A. Conde-Delmoral, C. M. Font Marin, G. Morell, Z. Chen and X. Wu, *Adv. Funct. Mater.*, 2024, *33*, 2407342.
15 S. Katiyar, S. Chang, I. Ullah, W. Hou, A. Conde-Delmoral, S. Qiu, G. Morell and X. Wu, *Energy Environ. Sci.*, 2024, **17**, 4770-4779.
16 S. Chang, W. Hou, A. Del Valle-Perez, I. Ullah, S. Qiu, J. L. Rodriguez, L. M. Díaz-Vázquez, L. Cunci, G. Morell and X. Wu, *Angew. Chem. Int. Ed.*, 2024, DOI: 10.1002/anie.202414346.
17 X. Zhao, N. Dong, M. Yan and H. Pan, *ACS Appl. Mater. Interfaces.*, 2023, **15**, 4053-4060
18 F. Wang, E. Hu, W. Sun, T. Gao, X. Ji, X. Fan, F. Han, X.-Q. Yang, K. Xu and C. Wang, *Energy Environ. Sci.*, 2018, **11**, 3168-3175.
19 Z. Xing, Y.-P. Deng, S. Sy, G. Tan, A. Li, J. Li, Y. Niu, N. Li, D. Su and J. Lu, *Nano Energy*, 2019, **65**, 104051.
20 H. Li, R. Zhao, W. Zhou, L. Wang, W. Li, D. Zhao and D. Chao, *JACS Au*, 2023, **3**, 2107-2116.
21 H. Liu, Z. Xin, B. Cao, Z. Xu, B. Xu, Q. Zhu, J. L. Yang, B. Zhang and H. J. Fan, *Adv. Funct. Mater.*, 2024, **34**, 2309840.
22 J. Hao, L. Yuan, C. Ye, D. Chao, K. Davey, Z. Guo and S. Z. Qiao, *Angew. Chem. Int. Ed.*, 2021, **60**, 7366-7375.
23 S. Lian, Z. Cai, M. Yan, C. Sun, N. Chai, B. Zhang, K. Yu, M. Xu, J. Zhu and X. Pan, *Angew. Chem.*, 2024, e202406292.
24 Z. Cai, J. Wang, S. Lian, J. Chen, F. Lang, Z. Li and Q. Li, *Adv. Funct. Mater.*, 2024, 2401367.
25 X. Wu, A. Markir, Y. Xu, C. Zhang, D. P. Leonard, W. Shin and X. Ji, *Adv. Funct. Mater.*, 2019, **29**, 1900911.
26 Z. He, F. Xiong, S. Tan, X. Yao, C. Zhang and Q. An, *Mater. Today Adv.*, 2021, **11**, 100156.
27 J. Liu, D. Dong, A. L. Caro, N. S. Andreas, Z. Li, Y. Qin, D. Bedrov and T. Gao, *ACS Cent. Sci.*, 2022, **8**, 729-740.
28 C. Bai, H. Jin, Z. Gong, X. Liu and Z. Yuan, *Energy Storage Mater.*, 2020, **28**, 247-254.
29 J. Zhao, X. Yang, S. Li, N. Chen, C. Wang, Y. Zeng and F. Du, *CCS Chem.*, 2021, **3**, 2498-2508.
30 M. Wang, Y. Meng, P. Gao, K. Li, Z. Liu, Z. Zhu, M. Ali, T. Ahmad, N. Chen and Y. Yuan, *Adv. Mater.*, 2023, **35**, 2305368.
31 S. Bi, S. Wang, F. Yue, Z. Tie and Z. Niu, *Nat. Commun.*, 2021, **12**, 6991.
32 Q. Yang, X. Qu, H. Cui, X. He, Y. Shao, Y. Zhang, X. Guo, A. Chen, Z. Chen and R. Zhang, *Angew. Chem. Int. Ed.*, 2022, **61**, e202206471.
33 S. Bi, Y. Zhang, S. Deng, Z. Tie and Z. Niu, *Angew. Chem. Int. Ed.*, 2022, **61**, e202200809.
34 M. Wang, Y. Meng, Y. Xu, N. Chen, M. Chuai, Y. Yuan, J. Sun, Z. Liu, X. Zheng and Z. Zhang, *Energy Environ. Sci.*, 2023, **16**, 5284-5293.
35 X. Wu, A. Markir, L. Ma, Y. Xu, H. Jiang, D. P. Leonard, W. Shin, T. Wu, J. Lu and X. Ji, *Angew. Chem. Int. Ed.*, 2019, **58**, 12640-12645.
36 C. Dai, L. Hu, H. Chen, X. Jin, Y. Han, Y. Wang, X. Li, X. Zhang, L. Song and M. Xu, *Nat. Commun.*, 2022, **13**, 1863.
37 J. Zhang, X. Zhang, C. Xu, H. Yan, Y. Liu, J. Xu, H. Yu, L. Zhang and J. Shu, *Adv. Energy Mater.*, 2022, **12**, 2103998.
38 G. Liang, F. Mo, Q. Yang, Z. Huang, X. Li, D. Wang, Z. Liu, H. Li, Q. Zhang and C. Zhi, *Adv. Mater.*, 2019, **31**, 1905873.

39 H. Cai, S. Bi, R. Wang, L. Liu and Z. Niu, *Angew. Chem. Int. Ed.*, 2022, **61**, e202205472.
40 F. Ambroz, T. J. Macdonald and T. Nann, *Adv. Energy Mater.*, 2017, **7**, 1602093.
41 G. A. Elia, K. Marquardt, K. Hoeppner, S. Fantini, R. Lin, E. Knipping, W. Peters, J. F. Drillet, S. Passerini and R. Hahn, *Adv. Mater.*, 2016, **28**, 7564-7579.
42 B. W. Zhang, L. Ren, Y. X. Wang, X. Xu, Y. Du and S. X. Dou, *Interdiscip. Mater.*, 2022, **1**, 354-372.
43 N. M. Laptash, E. V. Kovaleva, A. A. Mashkovskii, A. Y. Beloliptsev and L. A. Zemnukhova, *J. Struct. Chem.*, 2007, **48**, 848-854.
44 D. W. Barnum, *Inorg. Chem.*, 1983, **22**, 2297-2305.
45 S. Chang, J. F. F. Gomez, S. Katiyar, G. Morell and X. Wu, *J. Am. Chem. Soc.*, 2023, **145**, 24746-24754.
46 L. Jiang, Y. Lu, C. Zhao, L. Liu, J. Zhang, Q. Zhang, X. Shen, J. Zhao, X. Yu and H. Li, *Nat. Energy.*, 2019, **4**, 495-503.
47 Y. Li, W. Deng, Z. Zhou, C. Li, M. Zhang, X. Yuan, J. Hu, H. Chen and R. Li, *J. Mater. Chem. A*, 2021, **9**, 2822-2829.
48 Y. Xu, T. Ding, D. Sun, X. Ji and X. Zhou, *Adv. Funct. Mater.*, 2023, **33**, 2211290.
49 X. Zhang, T. Xiong, B. He, S. Feng, X. Wang, L. Wei and L. Mai, *Energy Environ. Sci.*, 2022, **15**, 3750-3774.
50 W. Ren, X. Chen and C. Zhao, *Adv. Energy Mater.*, 2018, **8**, 1801413.
51 D. Su, A. McDonagh, S.-Z. Qiao and G. Wang, *Adv. Mater.,* 2016, **29**.
52 Harris, D. C., *Quantitative Chemical Analysis*, 8th edn, W. H. Freeman, New York, 2010.
53 J. Zheng, D. C. Bock, T. Tang, Q. Zhao, J. Yin, K. R. Tallman, G. Wheeler, X. Liu, Y. Deng and S. Jin, *Nat. Energy*, 2021, **6**, 398-406.
54 J.-G. Zhang, W. Xu, J. Xiao, X. Cao and J. Liu, *Chem. Rev.,* 2020, **120**, 13312-13348.
55 Y. Liu, Y. Liu, X. Wu and Y.-R. Cho, *J. Colloid Interface Sci.* 2022, **628**, 33-40.
56 J. Peng, W. Zhang, Q. Liu, J. Wang, S. Chou, H. Liu and S. Dou, *Adv. Mater.*, 2022, **34**, 2108384.
57 Y. Li, J. Zhao, Q. Hu, T. Hao, H. Cao, X. Huang, Y. Liu, Y. Zhang, D. Lin and Y. Tang, *Mater. Today Energy*, 2022, 101095.
58 H. Yi, R. Qin, S. Ding, Y. Wang, S. Li, Q. Zhao and F. Pan, *Adv. Funct. Mater.*, 2021, **31**, 2006970.
59 G. Du and H. Pang, *Energy Storage Mater.*, 2021, **36**, 387-408.
60 X. Wu, Y. Xu, H. Jiang, Z. Wei, J. J. Hong, A. S. Hernandez, F. Du, X. Ji, *ACS Appl. Energy Mater.* 2018, **1**, 7, 3077-3083.
61 Z. Shadike, D.-R. Shi, M.-H. Cao, S.-F. Yang, J. Chen and Z.-W. Fu, *J. Mater. Chem. A.*, 2017, **5**, 6393-6398.
62 A. Zhou, L. Jiang, J. Yue, Y. Tong, Q. Zhang, Z. Lin, B. Liu, C. Wu, L. Suo and Y.-S. Hu, *ACS Appl. Mater. Interfaces.*, 2019, **11**, 41356-41362.
63 Z. Ren, D. Hu, X. Zhang, D. Liu and C. Wang, *Dalton Trans.*, 2019, **48**, 4058-4066.
64 C. Yang, S. Ding, Y. Zhao, J. Zhou, L. Li and J. Fan, *Dalton Trans.*, 2023, **52**, 16984-16992.
65 C. D. Wessells, R. A. Huggins and Y. Cui, *Nat. Commun.*, 2011, **2**, 550.
66 X. Liu, Y. Guo, F. Ning, Y. Liu, S. Shi, Q. Li, J. Zhang, S. Lu and J. Yi, *Nano-Micro Lett.*, 2024, **16**, 111.
67 L. Xiao, H. Lu, Y. Fang, M. L. Sushko, Y. Cao, X. Ai, H. Yang and J. Liu, *Adv. Energy Mater.*, 2018, **8**, 1703238.
68 C. Yang, Y. Zhao, J. Fan, L. Li, J. Zhou, K. Wang, F. Lu and H. Sun, *Mater. Adv.*, 2024.
69 S. Li, M. Xia, C. Xiao, X. Zhang, H. Yu, L. Zhang and J. Shu, *Dalton Trans.*, 2021, **50**, 6520-6527.
70 X. Wu, M. Shao, C. Wu, J. Qian, Y. Cao, X. Ai and H. Yang, *ACS Appl. Mater. Interfaces.*, 2016, **8**, 23706-23712.
71 F. Maroni, M. Li, S. Dongmo, C. Gauckler, M. Wohlfahrt‐Mehrens, M. Giorgetti and M. Marinaro, *ChemElectroChem.*, 2023, **10**, e202201070.
72 X. Wu, Y. Luo, M. Sun, J. Qian, Y. Cao, X. Ai and H. Yang, *Nano Energy*, 2015, **13**, 117-123.
73 Ni, Z. Hao, G. Y. Zou, F. H. Cao, L. Qin and C. G. Zhou, *ChemElectroChem*, 2022, **9**, e202101351.
74 G. Ni, M. Sun, Z. Hao, G. Zou, F. Cao, L. Qin, W. Chen and C. Zhou, *Mater. Today Energy*, 2023, **31**, 101204.
75 Q. Yang, F. Mo, Z. Liu, L. Ma, X. Li, D. Fang, S. Chen, S. Zhang and C. Zhi, *Adv. Mater.*, 2019, **31**, 1901521.
76 L. Cao, D. Li, T. Pollard, T. Deng, B. Zhang, C. Yang, L. Chen, J. Vatamanu, E. Hu and M. J. Hourwitz, *Nat. Nanotechnol.*, 2021, **16**, 902-910.
77 W. Zhou, D. Zhu, J. He, J. Li, H. Chen, Y. Chen and D. Chao, *Energy Environ. Sci.*, 2020, **13**, 4157-4167.

The data supporting this article have been included as part of the Supplementary Information.